Desalination and Water Treatment
www.deswater.com

doi: 10.1080/19443994.2016.1183233

57 (2016) 28450–28459
December

Taylor & Francis
Taylor & Francis Group

Improvement in TiO_2 photocatalytic performance by ZrO_2 nanocompositing and immobilizing

Hassan Koohestani[a,*], Sayed Khatiboleslam Sadrnezhaad[b]

[a]*Faculty of Materials and Metallurgical Engineering, Semnan University, Semnan, Iran, Tel. +98 23 33654100; Fax: +98 23 33321005; email: h.koohestani@semnan.ac.ir*
[b]*Department of Materials Science and Engineering, Sharif University of Technology, Azadi Ave., Tehran, Iran, email: sadrnezh@yahoo.com*

Received 6 January 2016; Accepted 21 April 2016

ABSTRACT

In this work, the effect of addition of ZrO_2 to TiO_2 and catalyst geometry on photocatalytic properties of the nanocomposite TiO_2/ZrO_2 was investigated. The traditional use of powdery photocatalyst for the degradation of organic compounds has post-treatment problems which means much higher time and costs. A novel method to minimize these problems is immobilization by insertion onto an inert substrate. Several geometries of TiO_2–10%ZrO_2 (T-10Z) nano-photocatalysts (powder, fiber, film, and network-shaped) were produced using different templates. The products were characterized by X-ray diffraction, field emission scanning electron microscopy, Brunauer–Emmett–Teller, and diffuse reflectance UV–vis spectra. Photocatalytic degradation of methyl orange in water was examined using TiO_2/ZrO_2 composites and T-10Z geometries under UV irradiation. The T-10Z with a band gap of 3.10 eV showed higher degradation than the other composites. The degradation rate of the four geometries produced was in the following order: powder > network > film > fiber. The rate constant of the dye degradation reaction when contacting with powdery and network composites were 0.019 and 0.013 min^{-1}, respectively. Network geometry with lower kinetic effects was preferred due to its indisputably higher immobility.

Keywords: TiO_2/ZrO_2 composite; Immobilized photocatalyst; Network structure; Microfiber; Dye degradation

1. Introduction

From long time ago, dyes have been used for coloring purposes in textile, paper, leather, food, and cosmetic industries. Release of dyes creates serious problems when discharged into the environmental systems like flowing streams or water supplies [1,2]. Fresh waters must remain clean and safe. A great deal of effort has been made in recent years to keep wastewaters away from natural sources of fresh water. Various catalytic techniques have been used to purify the dye containing polluted waters as well [3,4].

Recently, advanced oxidation processes (AOPs), based on the production of highly reactive hydroxyl radicals, have been proposed as an efficient method for the removal of different pollutants [5,6]. Heterogeneous photocatalysis based on semiconductors is the most famous AOP, in which irradiating the semiconductor by photons with sufficient energy with respect

*Corresponding author.

to the band gap energy of the semiconductor produces electron/hole pairs. The produced electron/holes can generate reactive hydroxyl or superoxide radicals by reaction of electron/hole with water and dissolved molecular oxygen, which can destroy different organic pollutants to smaller fragments and finally to water and CO_2 [6,7].

Semiconductors, such as TiO_2, are often used as catalytic agents because of their high stability, low cost, high efficiency, and no toxicity [1,8]. The values reported for the indirect band gap of crystalline rutile and anatase phases of TiO_2 are 3.0–3.2 eV, respectively. However, the practical applications of TiO_2 have been suppressed because of its two drawbacks. One of which is the rapid recombination of photo-induced electrons and holes and the other is the poor solar efficiency, which is determined by its band gap [1,6,9].

To improve the photocatalytic performance of titania, a number of studies have been carried out to couple titania with other materials like ZrO_2 [10]. ZrO_2 has a relatively high permittivity, large band gap (5.0–5.85 eV), and good thermal and chemical stability [11].

Mixed TiO_2/ZrO_2 has been widely investigated in the photocatalysis field. Nevertheless, the use of TiO_2/ZrO_2 nanoconjugates allows the creation of additional levels between TiO_2 valence and conduction bands which act as traps that retard the surface migration of the electron/hole pairs leading to a reactive migration to the surface and the corresponding desorption of the oxidized or reduced species. The addition of small amounts of ZrO_2 to TiO_2 can prevent the anatase-to-rutile phase transformation. Therefore, the addition of ZrO_2 enhances the thermal stability of pure TiO_2. Furthermore, ZrO_2 increases the surface area and promotes photocatalytic activity of TiO_2 in the form of OH groups [12–14].

Fu et al. have reported that 12 wt.% ZrO_2 is the optimum loading amount on TiO_2 for the photocatalytic degradation of ethylene using a 365 nm UV light source in which ZrO_2 by itself does not work as a photocatalyst, i.e. ZrO_2 is used only as a supporting material for TiO_2 [15].

Most studies dealing with photocatalytic degradation of water pollutants have used semiconductors applied in slurry form into the aqueous phase. However, the major disadvantage of slurry photocatalysis is the inefficient separation of the catalyst from purified water after treatment [1,4]. This problem has resulted in the development of several kinds of immobilization techniques to immobilize the photocatalyst powder, which may reduce the post-treatment expenses and time [4,8]. One way to make an immobile photocatalyst is to produce multidimensional structures such as thin-film, nanotube, nanowire, fiber, network, etc. which are fixed to the walls of the reaction reactor [8,16]. Various photocatalyst particle supports such as alumina, zeolite, silica gel, fiber optic cable, glass beads, quartz, stainless steels, clays, and activated carbon have been investigated [8,16,17].

Of the various geometries, network structure, a hollow three-dimensional structure has the potential for producing a new class of materials with novel applications. This structure is very important for practical applications because its pores has potentially large surface to volume ratio providing a significant advantage in the diffusion pathways which can be used as a kind of host for organic pollutants [4,18].

In the present study, the preparation of TiO_2/ZrO_2 composites and their effects on catalytic degradation of the methyl orange (MeO) color under UV light irradiation when contacted by powder, fiber, film, and network-shaped semiconductors were investigated. The structural and optical properties of the samples were studied by XRD, field emission scanning electron microscopy (FESEM), Brunauer–Emmett–Teller (BET), and UV–vis DRS spectra and then compared with each other.

2. Experimental procedure

2.1. Materials

Titanium (IV) isopropoxide (TTIP), zirconium oxychloride salt ($ZrOCl_2{\cdot}8H_2O$), ethanol (98%), ammonium hydroxide (NH_4OH), hydrochloricacid (HCl), 2-propanol, methyl orange (MeO) were purchased from MERCK manufacturer. Distilled water, cellulose fibers, and ceramic templates were obtained from local sources.

2.2. Synthesis

The TTIP and $ZrOCl_2{\cdot}8H_2O$ were used as titania and zirconia precursor for synthesizing TiO_2, ZrO_2, and TiO_2/ZrO_2 nanoparticles. The zirconia and titania precursor solutions were prepared separately.

2.2.1. Solution A

The titania precursor solution was obtained by mixing distilled water (85 mL), HCl (6 mL), and 2-propanol (6 mL) together. After thorough mixing at room temperature, titanium isopropoxide (5 mL) was gradually added to the solution. When the solution became clear it was stirred for 2 h at 60℃. The precipitate was prepared after many hours.

2.2.2. Solution B

The zirconia precursor solution was obtained by dissolving 10 mL of NH_4OH aqueous solution (2 M/L) in 25 mL of $ZrOCl_2{\cdot}H_2O$ (0.5 M/L). The mixture was stirred for 15 min at room temperature to produce a white gelatinous precipitate.

In order to obtain TiO_2/ZrO_2 nanocomposite, the precipitate solution A was added in solution B in which the ZrO_2 molar ratio was adjusted to many values (7.5, 10, 12.5, and 15%). Finally, all samples were calcined at 450˚C for 2 h in the furnace.

To prepare different geometries of T-10Z at first, the following layers were washed with distilled water and alcohol and then they were dried overnight. To produce the film, fiber and network geometries, 5 g of SiC plate, 0.2 g of cotton fiber and 4 g of hollow SiC foam were used. The substrates were immersed in the solution containing the T-10Z for one day. Then the prepared samples were washed to remove unabsorbed particles with DI water. After drying in the air, samples were calcined for 2 h at 450˚C to remove cotton and form rutile and anatase phases.

2.3. Characterization

The crystalline structure was obtained by a X-ray diffractometer (XRD, Spectro Xepos, Germany) with monochromated high-intensity Cu Kα radiation ($\lambda = 1.5418$ Å). Scherrer equation which is used to measure the crystal size according to the XRD pattern was adopted for the estimation of nanocrystalline size. The morphology of the samples was studied using a field-emission scanning electron microscope (FESEM, Mira 3-XMU, Czech).

The BET-specific surface area was determined by a Belsorp mini II (Japan) system. The diffusive reflectance spectra (DRS) of the samples were recorded with a UV–vis spectrophotometer (Avaspec-2048-TEC, Netherlands) using $BaSO_4$ as a reference in the region from 200 to 900 nm.

The room temperature photolumniscence (PL) analysis was carried out using Avaspec-2048-TEC (Netherlands) with an excitation wavelength at 355 nm.

2.4. Photocatalytic degradation

Catalytic activity of the samples was estimated from color degradation of the methyl orange aqueous solution (50 mL MeO of 5 mg/L initial concentration). The pH was maintained constant, equal to the initial pH of the MeO solution (i.e. 6.5). The same amount of catalyst was used (150 mg/L). Before irradiation with UV light, the aqueous solution which contained catalyst was continuously stirred for 1 h in full darkness to achieve adsorption–desorption equilibrium. UV irradiation from two 6 W lamp (254 nm-Philips, China) was then applied to the catalyst containing solution. The distance between the surface of the solution and the light source was 10 cm (Fig. 1). Samples were then taken out for analysis, every 30 min.

Solution concentration was determined by UV–vis spectrophotometer (Avaspec-2048-TEC). The maximum absorption wavelength registered for MeO was 462 nm.

3. Result and discussion

The XRD patterns of the pure TiO_2 samples calcined at 400–450˚C are displayed comparatively in Fig. 2. It can be observed that the crystalline structure of the sample calcined at 400˚C is of pure anatase phase. Calcination at 450˚C, by contrast, has resulted in a combination of anatase and rutile phases; hence an increase in the temperature has caused the rutile phase [19,20]. The rutile ratio (W_R) in terms of its weight fraction was directly calculated from the XRD intensity data using the following equation [4]:

$$W_R\% = \frac{1}{1 + 0.8\frac{I_R}{I_A}} \times 100 \quad (1)$$

where I_A and I_R represent the intensities of the strongest anatase ((1 0 1) peak at $2\theta = 25.4^\circ$) and the strongest rutile ((1 1 0) peak at $2\theta = 27.5^\circ$) reflections, respectively.

The XRD patterns of the TiO_2/ZrO_2 photocatalysts with various ZrO_2 to TiO_2 molar ratios calcined at 450˚C can be seen in Fig. 3. The significant peaks for ZrO_2 crystals can be observed at 24.5˚, 28.2˚, 31.6˚, etc. [21]. Table 1 summarizes XRD results of all the

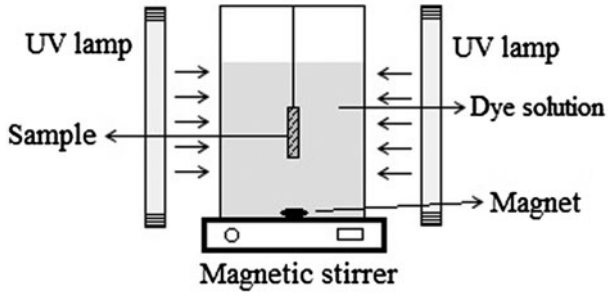

Fig. 1. Schematic diagram of photoreactor system.

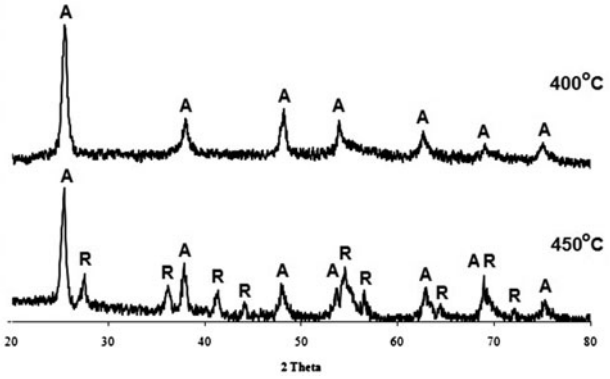

Fig. 2. XRD patterns of the synthesized TiO_2 calcined at 400–450˚C (A = Anatase TiO_2, R = Rutile TiO_2).

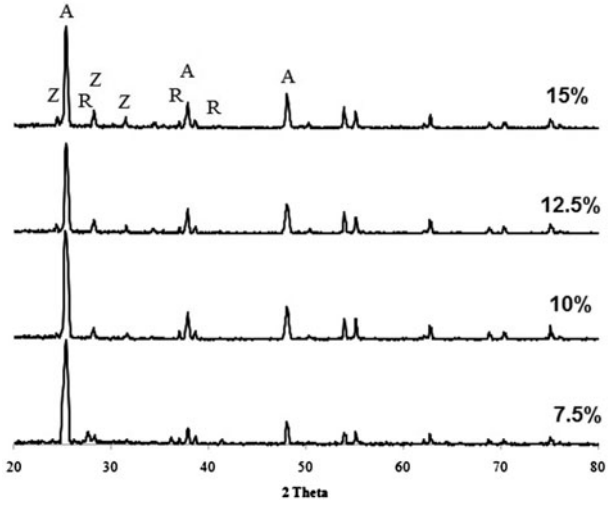

Fig. 3. XRD patterns of the synthesized TiO_2/ZrO_2 photocatalysts calcined at 450˚C (A = Anatase TiO_2, R = Rutile TiO_2, Z = ZrO_2).

synthesized powdery photocatalysts. It is observed that the presence of ZrO_2 has brought about some changes in the peaks intensities and the amount of anatase and rutile phases. In the sample of T-7.5Z, there is still small amount of rutile phase, but with the increase in the ratio of zirconia, rutile is removed from the structure due to increase in the transition temperature of anatase to rutile [12,13]. The results suggest that the ZrO_2 incorporation tended to cause the change in crystallite size of the anatase phase and the smallest size was obtained in 10% Z.

Fig. 4 indicates FESEM images of pure TiO_2 and T-10Z nanoparticles calcined at 450˚C. TiO_2 particles in Fig. 4(a) have near spherical agglomerated shape in the size range of 20–40 nm. Fig. 4(b) illustrates T-10Z. Although size measurement is slightly difficult from the image due to agglomeration of particles, we can conclude that the size of the particles is 20–70 nm.

FESEM image of the T-10Z film is shown in Fig. 5(a). As it can be observed, the particles in the size range of 20–60 nm on the surface of the substrate is covered by a relatively uniform. The thickness of the film is 10–12 μm (top right of Fig. 5(a)). At bottom right of Fig. 5(a), an EDX diagram of film sample is illustrated. According to the substrate SiC, there are three elements on the surface: oxygen, zirconium and titanium. T-10Z microfibers shown in Fig. 5(b) are 20 μm long hollow cylinders having 0.2–0.6 μm diameters (top right of Fig. 5(b)). They were produced by template-coating and removal of the cellulose base by subsequent heat treatment. According to the EDX analysis in bottom right of Fig. 5(b), only Ti, Zr, and O presence in the annealed samples are detected. Therefore, calcination at 450˚C led to the removal of all the cellulose which was used.

Fig. 5(c) illustrates the T-10Z particles deposited on the wall of the network shape substrate. An image of network is shown in top right of Fig. 5(c). The deposited layer has a thickness of less than 10 μm. By studying the EDX diagram in bottom right of Fig. 5(c), the presence of O, Zr, and Ti is confirmed.

The BET-specific surface areas of pure TiO_2, different TiO_2/ZrO_2 composites and four geometries of T-10Z calcined at 450˚C are listed in Table 2. This can

Table 1
XRD results of the powder synthesized pure TiO_2 and TiO_2/ZrO_2 photocatalysts

Photocatalyst	Abbreviated name	Rutile ratio, W_R	Crystallite size (nm)	
			Anatase (1 0 1)	Rutile (1 1 0)
TiO_2, 400˚C	T400	0	16.7	–
TiO_2, 450˚C	T450	31.0%	16.4	19.7
TiO_2–7.5% ZrO_2	T-7.5Z	12.2%	17.6	18.7
TiO_2–10% ZrO_2	T-10Z	0	16.2	–
TiO_2–12.5% ZrO_2	T-12.5Z	0	16.9	–
TiO_2–15% ZrO_2	T-15Z	0	17.4	–

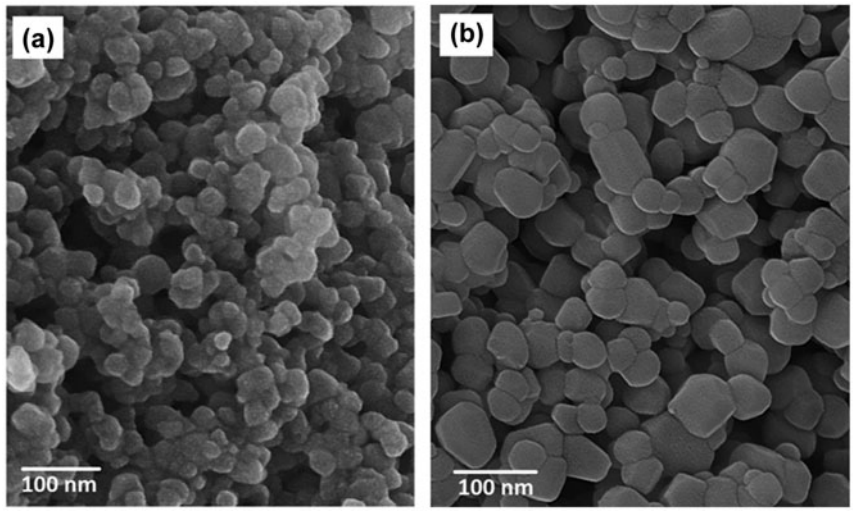

Fig. 4. FESEM images of (a) pure TiO_2 and (b) T-10Z nanoparticles calcined at 450°C.

be ascribed to the effect of crystallite size on BET surface area. It is well known that crystallite size is an important parameter for catalysis in general since it directly impacts on the specific surface area of a catalyst [22].

It can be clearly observed that the addition of ZrO_2 resulted in an increase in the specific surface area. Particularly, by incorporating 10% ZrO_2 in the pure TiO_2, the specific surface area increased from 68.2 to 85.5 $m^2 g^{-1}$ at a calcination temperature of 450°C. This is possibly because the incorporation of this second metal oxide with proper amounts can retard the crystallization process of the photocatalysts, thus slowing down the growth of photocatalyst grain size and resulting in higher specific surface areas of the mixed oxide photocatalysts [22,23].

Powdery geometry has the highest surface area among the four geometries of T-10Z and after that network geometry has greater specific surface area (47.5 $m^2 g^{-1}$). In the coated samples (film and network), due to the agglomeration of the particles, the surface area decreased and the average particle size increased [4,6]. In fact, the surface area of the catalyst is minimized since the coating layer has a lower porosity. Due to the accumulation of fibers and closure of some of them, the surface area of the fiber sample is greatly reduced [8,17].

The photocatalytic performance of a semiconductor significantly depends on its optical property, and thus, it is one of the important factors which should be studied. Fig. 6 shows typical UV–vis diffuse reflectance spectroscopy (UV–vis DRS) curves for optical absorption behavior of TiO_2/ZrO_2 samples. The optical transitions in semiconductor materials are believed to take place via direct and indirect transitions which can be studied using the following Kubelka–Munk equation [6,24]:

$$(\alpha h\nu) = \beta\left(h\nu - E_g\right)^n \tag{2}$$

where E_g is the energy band gap of semiconductors (eV), ν is the frequency of light (s^{-1}), h is the Planck's constant (J.s), β is the absorption constant, and α is the absorption coefficient defined by the Beer–Lambert law as $\alpha = ([2.303 \times Abs]/d)$, where d and Abs are the sample thickness and sample absorbance, respectively. For precise determination of α, some corrections should be made to the absorption due to reflection. In this equation, index n has different values of 1/2, 2, 3/2, and 3 for allowed direct, allowed indirect, forbidden direct and forbidden indirect electronic transitions [6,24].

The band gap can be determined by extrapolating of the linear portion of the $(\alpha h\nu)^n - h\nu$ curve. The best linear fitting was obtained for the $(\alpha h\nu)^2 - h\nu$ curve for the TiO_2/ZrO_2 catalyst which is in accordance with the literature for both semiconductors [25,26].

Table 2 summarizes the results of band gap energy of all the photocatalysts obtained from the UV–vis absorption spectra and Eq. (2). As indicated, the band gap for the as-prepared TiO_2 is 2.95 eV. It is observed that the light absorption exhibited significant blue shifts by the incorporation of ZrO_2 into TiO_2 [13,21]. The band gaps calculated for 7.5, 10, 12.5, and 15% ZrO_2 were found to be 3.07, 3.10, 3.12, 3.18 eV, respectively. Then, the presence of ZrO_2 increased the band gap energy and shortened the threshold wavelength.

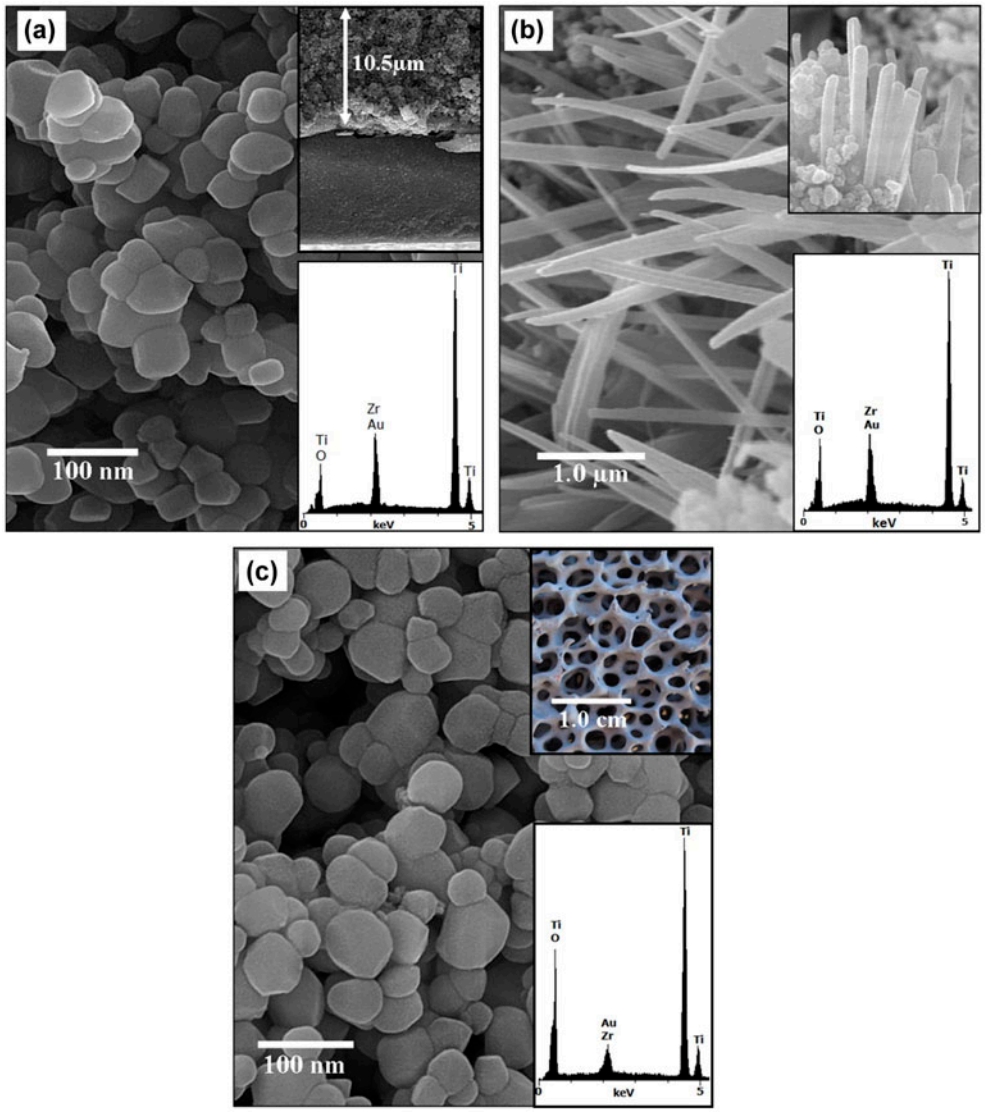

Fig. 5. Geometries of T-10Z: (a) FESEM image, crosssection and EDX of Film, (b) FESEM images and EDX of Fiber, and (c) FESEM image, photo and EDX of Network geometry.

Table 2
Specific surface areas and band gap energy of samples calcined at 450°C

Photocatalyst	State	S_{BET} (m^2/g)	Band gap energy, E_g (eV)
Pure TiO_2	Powder	68.2	2.95
T-7.5Z	Powder	81.2	3.07
T-12.5Z	Powder	76.3	3.12
T-15Z	Powder	67.4	3.18
T-10Z	Powder	85.5	3.10
	Fiber	44.6	–
	Film	46.4	–
	Network	47.5	–

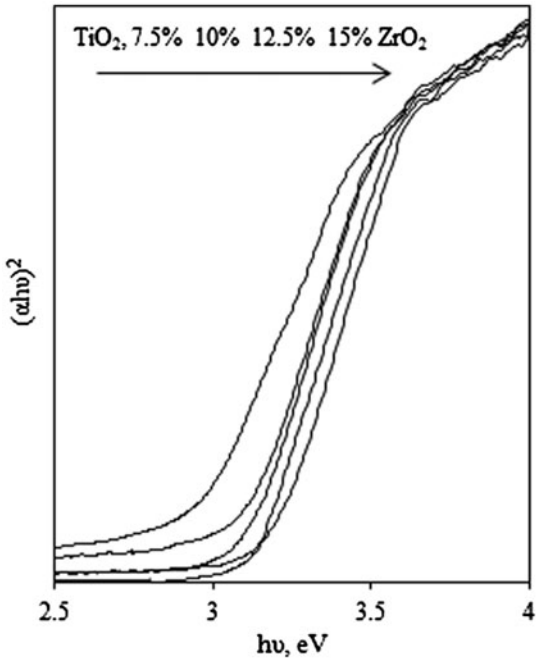

Fig. 6. The corresponding Kubelka–Munk function spectra to determine direct new band gap values for the synthesized TiO_2/ZrO_2 photocatalysts with variation of ZrO_2 content.

The PL emission is directly related to the recombination of excited electrons and holes, so the lower PL intensity indicates a delay in recombination rate and, thus, higher photocatalytic activity [27]. As shown in Fig. 7, the T-10Z had the lower recombination rate of electrons and holes.

The conduction band (CB) surface trap state of ZrO_2 is around 1.3 eV higher than that of pure TiO_2. The formation of such surface states of ZrO_2 and TiO_2 has been described by Ghosh et al. [26]. These results

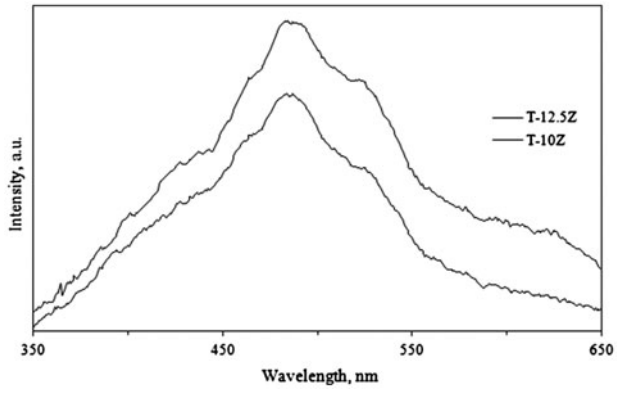

Fig. 7. Photoluminescence of T-10Z and T-12.5Z powders.

are a clear indication of the injection of electrons from the surface states of ZrO_2 to TiO_2. In the case of ZrO_2 loaded to TiO_2, the PL intensity decreased by the addition of 10 wt.% ZrO_2 and, the excited electrons are completely injected into TiO_2, leading to an enhancement of dye degradation for the T-10Z.

Photodegradation of MeO using TiO_2 and different molar ratios of TiO_2/ZrO_2 calcined at 450˚C under UV light irradiation are illustrated in Fig. 8(a). The T-10Z sample shows better photocatalytic performance than the other composites or TiO_2. After 210 min of UV-illumination, the MeO removal over TiO_2 is only 87%. However, the MeO removals over TiO_2/ZrO_2 composites are 76–98%. As reported by Fu et al. electron and hole separation may take place between ZrO_2 and TiO_2 in the binary oxide [15] since the energy level of TiO_2 both for the valence band and conduction band correspond well within the band gap of ZrO_2. When the electrons are excited from both catalysts, most of the electrons from the CB of ZrO_2 can easily transfer to the CB of TiO_2 and, thereby, the electron/hole recombination may be prevented in ZrO_2 loaded to TiO_2.

Among these photocatalysts, T-10Z reveals the most efficacious performance. The photocatalytic performance of other composites is not as good as T-10Z, especially under light irradiation. The high photocatalytic activities can be attributed to the small crystallite size, the large specific surface area, and the low band gap energy. Conclusively, the use of the T-10Z photocatalyst can provide a much higher number of surface active sites (implying a significant decrease in the number of lattice defects) and consequently facilitate the electron transport after the band gap photoexcitation for reacting with water molecules adsorbed on its surface active sites along the mesoporous-assembled structure [28].

In Fig. 8(b), the removal of MeO from its aqueous solution by different geometries of T-10Z is plotted against irradiation time of UV rays. Powder geometry photocatalyst reduced the MeO concentration faster than the other geometries. The relation between MeO degradation rate and photocatalyst geometries follows the sequence: Powder > Network > Film > Fiber. After powdery sample, the network sample has faster dye degradation than other geometries. After 210 min of UV-illumination, the MeO removal over fiber and film are 81–88%, respectively. However, the MeO removal over network is as high as 94%. This superiority of network sample over the other two immobilized geometries may be due its higher specific area compared to that of the other two [8,17]. Therefore, the geometry of photocatalyst plays an important role in the photocatalytic reaction.

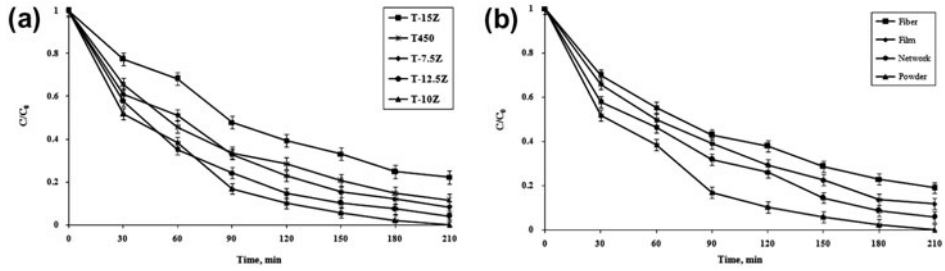

Fig. 8. Photodegradation of MeO by (a) pure TiO_2 and TiO_2/ZrO_2 mixed oxides calcined at 450˚C and (b) various geometry of T-10Z.

Recently, the kinetic of various organic compounds such as organic dyes have been investigated. Many researchers reported that the photocatalytic degradation of organic compounds can be simply fitted to pseudo-first-order kinetics [1,4,10].

However, the reaction kinetic is affected by the initial organic content so that the pseudo-first-order kinetics is only applicable when the concentration of organic content is low. Thus, a heterogeneous Langmuir–Hinshelwood kinetic model is generally used [1,2]. For a general first-order reaction, the equation relating the k_{app} which is the apparent-first-order reaction rate constant (min^{-1}), C_0 which is the initial concentration of MeO dye in the bulk solution (mg/L) and t is the reaction time (min) is given as [6,29]:

$$r = -\frac{dC}{dt} = k_{app}C \tag{3}$$

$$\ln\left(\frac{C_0}{C}\right) = k_{app}t \tag{4}$$

The reaction kinetics of the photocatalytic degradation of the MeO dye under UV light was also studied. A plot of $\ln(C_0/C)$ vs. t for all the experiments with same initial concentration of MeO is shown in Fig. 9. The values of degradation rate constant (k_{app}) can be gained directly from the regression analysis of the linear curve in the plot. k_{app} of the MeO dye in Table 3 was obtained from the data given in Fig. 9(a) and (b). The linear regression coefficients (R^2) were relatively high, indicating that the photocatalytic decolorization of MeO obeys the Langmuir–Hinshelwood (first-order) kinetic model.

It can be easily found that with the increase in ZrO_2 concentrations, the apparent rate constant firstly increased from 0.012 min^{-1} at 7.5% to 0.019 min^{-1} at 10%, and then decreased to 0.007 min^{-1} at 15%. The effect of geometry on the photocatalytic degradation kinetic of MeO was also investigated in Fig. 9(b). It is evident that the degradation kinetic of different geometries is not equal. The rate constants of fiber and film geometries are around 0.008–0.010 min^{-1}, while the rate constant of network geometry is 0.013 min^{-1}. As a result, the rate constants at the same initial condition are powder > network > film > fiber geometry.

For a solid–liquid adsorption process, the solute transfer is usually characterized by external mass transfer or intra-particle diffusion or both. The most widely applied intra-particle diffusion equation for

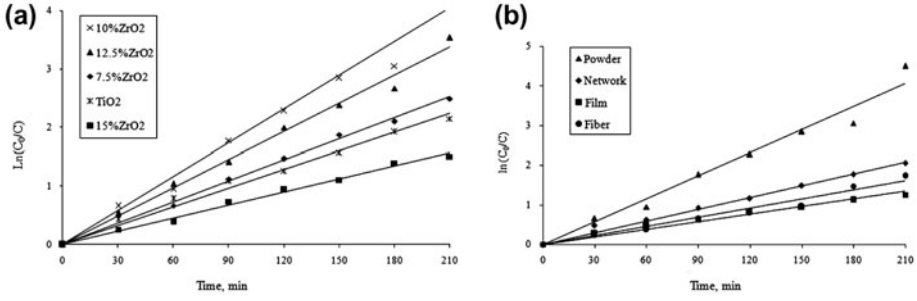

Fig. 9. Kinetics of MeO photodegradation (a) pure TiO_2 and TiO_2/ZrO_2 mixed oxides calcined at 450˚C and (b) various geometry of T-10Z.

Table 3
Kinetic parameters of MeO photodegradation by various photocatalysts

Photocatalyst	State	Lungmuir–Hinshelwood model		Weber–Morris model	
		Rate constant (min^{-1})	R^2	k_{id} ($mg/g.min^{0.5}$)	R^2
Pure TiO_2	450℃	0.010	0.984	–	–
T-7.5Z	Powder	0.012	0.993	–	–
T-12.5Z	Powder	0.016	0.990	–	–
T-15Z	Powder	0.007	0.991	–	–
T-10Z	Powder	0.019	0.986	0.545	0.988
	Fiber	0.008	0.983	0.274	0.978
	Film	0.010	0.990	0.393	0.501
	Network	0.013	0.985	0.455	0.970

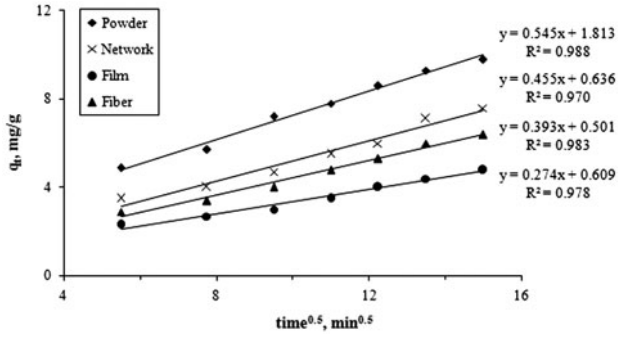

Fig. 10. Weber–Morris intra-particle diffusion plots for the adsorption of MeO on various geometries of T-10Z.

sorption system is given by Weber and Morris as follows [30,31]:

$$q_t = k_{id} t^{0.5} + C \quad (5)$$

where k_{id} ($mg/g\ min^{0.5}$) is the rate constant of the intra-particle diffusion model and C (mg/g) reflects the boundary layer effect [30]. The k_{id} and C can be determined from the slope and intercept of the linear plot of q_t against $t^{0.5}$ shown in Fig. 10. The kinetic model parameters at different geometries were summarized in Table 3.

When the plots do not pass through the origin, this is indicative of some degree of boundary layer control and this further show that the intra-particle diffusion is not the only rate-limiting step, but also other kinetic models may control the rate of adsorption, all of which may be operating simultaneously [31–33]. From the plot, it is observed that the lines did not pass through the origin. This indicated that the rate-limiting process is not only governed by intra-particle diffusion. Some other mechanism along with intra-particle diffusion was involved [30,31].

4. Conclusions

In summary, a series TiO_2–ZrO_2 composite photocatalysts have been successfully synthesized. After studying the results of the performed analyses, a suitable ZrO_2 incorporation of 10% was found to provide the enhanced photocatalytic MeO degradation. The T-10Z with a band gap energy of 3.10 eV showed high MeO degradation (98% for 210 min). Then four geometries of T-10Z (powder, fiber, film, and network) were produced on to substrates. Network geometry with surface area of 47.5 $m^2\ g^{-1}$ had higher degradation rate than other immobilized samples.

References

[1] A.H. Jawad, A.F. Alkarkhi, N.S.A. Mubarak, Photocatalytic decolorization of methylene blue by an immobilized TiO2 film under visible light irradiation: Optimization using response surface methodology (RSM). Desalin. Water Treat. 56(1) (2015) 161–172.
[2] N. Puvaneswari, J. Muthukrishnan, P. Gunasekaran, Toxicity assessment and microbial degradation of azo dyes, Indian J. Exp. Biol. 44(8) (2006) 618–626.
[3] J. Yu, Y. Su, B. Cheng, M. Zhou, Effects of pH on the microstructures and photocatalytic activity of mesoporous nanocrystalline titania powders prepared via hydrothermal method, J. Mol. Catal. A: Chem. 258 (1–2) (2006) 104–112.
[4] H. Koohestani, S.K. Sadrnezhaad, Photocatalytic activity of immobilized geometries of TiO_2, J. Mater. Eng. Perform. 24(7) (2015) 2757–2763.
[5] A. Nezamzadeh-Ejhieh, M. Bahrami, Investigation of the photocatalytic activity of supported ZnO–TiO_2 on clinoptilolite nano-particles towards photodegradation of wastewater-contained phenol, Desalin. Water Treat. 55(4) (2015) 1096–1104.
[6] H. Koohestani, S.K. Sadrnezhaad, Photocatalytic degradation of methyl orange and cyanide by using TiO_2-CuO composite, Desalin. Water Treat., doi: 10.1080/19443994.2015.1132395.
[7] S. Asl, S. Sadrnezhaad, M. Kianpoor rad, Photocatalytic decolorization of red dye in aqueous ZnO-TiO_2 suspensions, Adv. Mater. Res. 55–57 (2008) 577–580.

[8] H. Koohestani, S.K. Sadrnezhaad, A. Kheilnejad, Investigation of photocatalytic performance of TiO_2 network and fiber geometries, Desalin. Water Treat., doi: 10.1080/19443994.2015.1136965.
[9] L.-R. Hou, C.-Z. Yuan, Y. Peng, Synthesis and photocatalytic property of SnO_2/TiO_2 nanotubes composites, J. Hazard. Mater. 139(2) (2007) 310–315.
[10] X. Zhang, Q. Liu, Visible-light-induced degradation of formaldehyde over titania photocatalyst co-doped with nitrogen and nickel, Appl. Surf. Sci. 254(15) (2008) 4780–4785.
[11] M. Dong, H. Wang, C. Ye, L. Shen, Y. Wang, J. Zhang, J. Zhang, Y. Ye, Structure and electrical properties of sputtered TiO_2/ZrO_2 bilayer composite dielectrics upon annealing in nitrogen, Nanoscale Res. Lett. 7(1) (2012) 1–5.
[12] K. Maver, U.L. Stangar, U. Cernigoj, S. Gross, R.C. Korosec, Low-temperature synthesis and characterization of TiO_2 and TiO_2-ZrO_2 photocatalytically active thin films, Photochem. Photobiol. Sci. 8(5) (2009) 657–662.
[13] J.Y. Kim, C.S. Kim, H.K. Chang, T.O. Kim, Synthesis and characterization of N-doped TiO_2/ZrO_2 visible light photocatalysts, Adv. Powder Technol. 22(3) (2011) 443–448.
[14] Y. Wan, J. Ma, W. Zhou, Y. Zhu, X. Song, H. Li, Preparation of titania–zirconia composite aerogel material by sol-gel combined with supercritical fluid drying, Appl. Catal. A 277(1–2) (2004) 55–59.
[15] X. Fu, L.A. Clark, Q. Yang, M.A. Anderson, Enhanced photocatalytic performance of titania-based binary metal oxides: TiO_2/SiO_2 and TiO_2/ZrO_2, Environ. Sci. Technol. 30(2) (1996) 647–653.
[16] N. Alenzi, W.S. Liao, P.S. Cremer, V.S. Torres, T.K. Wood, C.E. Economides, Z. Cheng, Photoelectrochemical hydrogen production from water/methanol decomposition using Ag/TiO_2 nanocomposite thin films, Int. J. Hydrogen Energy 35(21) (2010) 11768–11775.
[17] H. Koohestani, S.K. Sadrnezhaad, The influence of structures on the TiO_2 photocatalystic properties, in: M. Reza Ejtehadi (Ed.), 5th International Conference on Nanostructures (ICNS5), 507–509.
[18] X. Zhang, C. Hu, H. Bai, Y. Yan, J. Li, H. Yang, X. Lu, G. Xi, Construction of Self-Supported Three-Dimensional TiO_2 Sheeted Networks with Enhanced Photocatalytic Activity, Scientific reports 3 (2013) 3563, 6 pp.
[19] K.J.A. Raj, B. Viswanathan, Effect of surface area, pore volume and particle size of P25 titania on the phase transformation of anatase to rutile, Indian J. Chem. A 48 (2009) 1378–1382.
[20] L. Andronic, D. Andrasi, A. Enesca, M. Visa, A. Duta, The influence of titanium dioxide phase composition on dyes photocatalysis, J. Sol-Gel Sci. Technol. 58(1) (2011) 201–208.
[21] B. Neppolian, Q. Wang, H. Yamashita, H. Choi, Synthesis and characterization of ZrO_2–TiO_2 binary oxide semiconductor nanoparticles: Application and interparticle electron transfer process, Appl. Catal. A 333(2) (2007) 264–271.
[22] W. Zhou, K. Liu, H. Fu, K. Pan, L. Zhang, L. Wang, C.C. Sun, Multi-modal mesoporous TiO_2-ZrO_2 composites with high photocatalytic activity and hydrophilicity, Nanotechnology 19(3) (2008) 035610, 7 pp.
[23] B. Mahipal, B.M. Reddy, S. Mehdi, Reactivity of V_2O_5 with TiO_2-ZrO_2, mixed oxide: An X-ray diffraction study, J. Solid State Chem. 97 (1992) 233–238.
[24] Z. Khodami, A. Nezamzadeh-Ejhieh, Investigation of photocatalytic effect of ZnO-SnO_2/nano clinoptilolite system in the photodegradation of aqueous mixture of 4-methylbenzoic acid/2-chloro-5-nitrobenzoic acid, J. Mol. Catal. A: Chem. 409 (2015) 59–68.
[25] L. Liang, Y. Sheng, Y. Xu, D. Wu, Y. Sun, Optical properties of sol-gel derived ZrO_2-TiO_2 composite films, Thin Solid Films 515(20–21) (2007) 7765–7771.
[26] N. Smirnova, Y. Gnatyuk, A. Eremenko, G. Kolbasov, V. Vorobetz, I. Kolbasova, O. Linyucheva, Photoelectrochemical characterization and photocatalytic properties of mesoporous TiO_2/ZrO_2 films, Int. J. Photoenergy 2006 (2006) 1–6.
[27] K. Gupta, R.P. Singh, A. Pandey, A. Pandey, Photocatalytic antibacterial performance of TiO_2 and Ag-doped TiO_2 against *S. aureus*. *P. aeruginosa* and *E. coli*, Beilstein J. Nanotechnol. 4(1) (2013) 345–351.
[28] T. Sreethawong, Y. Suzuki, S. Yoshikawa, Synthesis, characterization, and photocatalytic activity for hydrogen evolution of nanocrystalline mesoporous titania prepared by surfactant-assisted templating sol-gel process, J. Solid State Chem. 178(1) (2005) 329–338.
[29] T. An, J. An, H. Yang, G. Li, H. Feng, X. Nei, Photocatalytic degradation kinetics and mechanism of antivirus drug-lamivudine in TiO_2 dispersion, J. Hazard. Mater. 197 (2011) 229–236.
[30] N. Krishnan, M. Ilayaraja, R. Karthik, R.S. Kannan, Spectroscopic analysis of crystal violet dye removal by sida rhombifolia: Kinetic, equilibrium, thermodynamic studies, World J. Pharm. Pharm. 3 (2014) 713–732.
[31] N. Oladoja, C. Aboluwoye, Y. Oladimeji, Kinetics and isotherm studies on methylene blue adsorption onto ground palm kernel coat, Turk. J. Eng. Environ. Sci. 32(5) (2009) 303–312.
[32] Z.Z. Chowdhury, S.M. Zain, R.A. Khan, K. Khalid, Linear regression analysis for kinetics and isotherm studies of sorption of manganese (II) ions onto activated palm ash from waste water, Orient. J. Chem 27 (2011) 405–415.
[33] A. Itodo, F.W. Abdulrahman, L.G. Hassan, S.A. Maigandi, H.U. Itodo, Intraparticle diffusion and intraparticulate diffusivities of herbicide on derived activated carbon, Researcher 2(2) (2010) 74–86.